Available online at www.sciencedirect.com

ScienceDirect

Ceramics International 40 (2014) 3053–3061

CERAMICS INTERNATIONAL

www.elsevier.com/locate/ceramint

Toughness control of boron carbide obtained by spark plasma sintering in nitrogen atmosphere

Petre Badica[a,b,c], Hanna Borodianska[a,b], Shumao Xie[a], Ting Zhao[a], Dmytro Demirskyi[b], Peifeng Li[a], Alfred I.Y. Tok[a], Yoshio Sakka[b], Oleg Vasylkiv[a,b,*]

[a]Nanyang Technological University, 50 Nanyang Avenue, 639798 Singapore, Singapore
[b]National Institute for Materials Science, 1-2-1, Sengen, Tsukuba, Ibaraki 305-0047, Japan
[c]National Institute of Materials Physics, Atomistilor 105bis, Magurele 077125, Romania

Received 20 August 2013; received in revised form 30 September 2013; accepted 30 September 2013
Available online 8 October 2013

Abstract

Boron carbide ceramic was prepared by reactive Spark Plasma Sintering under N_2-atmosphere and for different heating times and maximum pressure regimes. Split-Hopkinson Pressure Bar (SHPB), indentation, XRD and microscopy measurements were performed for samples characterization. It is shown that SHPB toughness control depending on SPS regime is possible and the main reason is introduction of nitrogen into B_4C ceramic. Complex relationships between processing conditions, sintering mechanism, material's specifics, static and dynamic mechanical properties are discussed. Improvement of dynamic toughness is through mechanisms resembling those working for static load conditions such as cracks deflection and pull out, but there are also significant differences.

Keywords: C. Hardness; Boron carbide; SPS; Toughness; SHPB

1. Introduction

Boron carbide (B_4C) is a hard, light-weight, refractory and stable compound useful for different applications [1–3]. Further investigation and development of B_4C-based materials is of much interest. The biggest challenge is to improve toughness of B_4C-based ceramic well known to be a brittle material. Many applications require good mechanical properties under static, dynamic or impact strain-rate mechanical load regimes [4]. A simple and popular strategy for ceramics in general is to generate composites [5,6]. Improvement of toughness usually refers to fracture toughness, i.e. K_{1c}, determined in the static stress–strain load regime and very few data are available for B_4C-based composites in the dynamic or impact regions.

In this work, we present Split-Hopkinson Pressure Bar (SHPB) compressive test and Vickers indentation results on B_4C-based composite ceramic produced by reactive Spark Plasma Sintering (SPS) in N_2 atmosphere and under different regimes (Table 1). Selection of SPS was made considering literature data showing that pulsed current application during SPS processing may generate useful unconventional effects [7] leading to different results [8,9] when compared with resembling hot-pressing that applies conventional heating inside an electrical furnace. In our recent article [10] we have shown that reactive SPS of B_4C in N_2-atmosphere produces a composite in which at grain boundaries a fine mesh-like network of BN (with hexagonal crystal structure according to XRD) wrapped and intercalated by B_xO_y forms. Modified boundaries are expected to provide ductility to B_4C-based composite. Our work demonstrates that through different SPS regimes, the composite can be controlled from the viewpoint of dynamic (SHPB) maximum stress (σ_{max}), maximum strain (ε_{max}) and toughness (S) (Table 1).

2. Experimental

Powder of B_4C (Sinopharm Chemical Reagent Co. Ltd., Singapore, BET specific surface area and average particle size

*Corresponding author at: National Institute for Materials Science, 1-2-1, Sengen, Tsukuba, Ibaraki, 305-0047, Japan.
E-mail addresses: oleg.vasylkiv@nims.go.jp, ovasylkiv@ntu.edu.sg (O. Vasylkiv).

0272-8842/$ - see front matter © 2013 Elsevier Ltd and Techna Group S.r.l. All rights reserved.
http://dx.doi.org/10.1016/j.ceramint.2013.09.141

Table 1
Samples, SPS regime, static and dynamic mechanical properties parameters, optical microscopy results on samples after SHPB test and crystallite size from XRD.

S	Pressure, P [MPa], (atmosphere) and SPS time [min]	HV [GPa]	K_{Ic} [MPa.m$^{1/2}$]	SHPB max stress, σ_{mas} [MPa]	SHPB max. Strain ϵ_{max}	SHPB toughness from area S [MJ/m^2]	n-value	Observations from the optical microscopy after SHPB test (see Fig. 2 a–f)	Crystallite size from XRD [nm]
U	60 (Ar)/ 6 min	22.51	2.21	740	0.0117	6.50	–	Relatively uniform fraction of middle size fractured pieces	101
V	60 (N2)/ 6 min	34.9	4.56	1223	0.0209	18.33	–	Relatively uniform fraction of small size fractured pieces	111
Z	60 (N2/20 min to 1100C and 5 min to 1800C in Ar)	24.4	6.13	522	0.0278	10.44	–	Relatively uniform fraction of small size fractured pieces	99.8
A1	30/(N2) 25 min	27.4	3.17	713	0.0134	6.52	1.50	Relatively uniform fraction of middle size fractured pieces	163
A2	30/(N2) 25 min	–	–	723	0.0124	5.77	–		
B1	60/(N2) 25 min	35.6	4.18	925	0.0209	12.95	2.39	Two fractions very different: 1. Few very large pieces	146
B2	60/(N2) 25 min	–	–	1185	0.0199	14.22	–	2. Fraction of small pieces	
C1	100/(N2) 25 min	34	5.31	1014	0.0598	29.83	2.37	Two fractions very different: 1. Needle-like pieces	131
C2	100/(N2) 25 min	–	–	1270	0.0593	30.93	–	2. Signicant fraction of very small pieces.	
A*	30/(N2) 40 min	24.8	7.55	701	0.0338	15.04	2.32	Two fractions: 1. Relatively uniform fraction of middle size fractured pieces as for A1, 2 2. Fraction of very small particles as for C1, 2	99
B*	60/(N2) 40 min	35.2	6.18	1153	0.0319	20.70	2.37	Two fractions: 1. Relatively uniform fraction of middle size fractured pieces as for A1, 2 2. Fraction of very small particles as for C1, 2	108

of the powder, given by the manufacturer, were 15.79 m^2/g and 1 μm. Our microscopy observations revealed particles with sizes from 0.1 to 5 μm. Powder was processed by SPS-Syntex equipment (Japan) using graphite mold systems. For each sample, maximum pressure (30, 60 or 100 MPa), atmosphere (Ar or N_2) and heating time (25 or 40 min) up to a maximum SPS temperature of 1800 °C, are presented in Table 1. The initial weight of the powder was constant. Molds with inner diameter of 10 mm were used. Height of cylindrical samples was 6 mm after polishing their surfaces. Two identical samples of A, B and C were obtained and denoted as 1 and 2.

Uniaxial dynamic compression tests on B_4C specimens at high strain rates of 1000 s^{-1} were conducted using a SHPB system available at NTU, Singapore. The system consists of 20 mm diameter YAG300 maraging steel striker (length 400 mm), incident (length 1200 mm) and transmitted (length 1200 mm) bars. Both incident and transmitted bars were instrumented with TML strain gauges (Tokyo Sokki Kenkyujo Co. Ltd., Japan, gauge factor of 2.11). Signals from strain gauges were used to calculate the stress and strain history based on the one-dimensional elastic bar wave theory for a pulse propagating in a uniform bar (SHPB theory) [11]. Hardened high strength steel platens, whose impedance matched that of the bars, were sandwiched between the bars and specimens to prevent the indentation of the bars [12]. Dynamic (SHPB) toughness, S, is defined as the area below the strain–stress curve up to ε_{max}.

Vickers indentations were performed for 1Kg load (Future-Tech FM-300e, Japan) and results are averaged for at least 10 measurements. Static fracture toughness was calculated as: $K_{1c}=9.052\times10^{-3}(HV)^{3/5}Y^{2/5}dl^{-1/2}$, where HV is Vickers hardness, Y is Young's modulus, d is the average diagonal line length of the indentation print, and l is the average length of the cracks [13].

Samples after SPS and after SHPB test were observed by scanning electron microscopy using a JEOL JSM-7600F, Japan equipped with energy dispersive system (EDS). A TEM microscope (JEOL JEM 2100F, Japan) was also used. Optical microscopy was also employed to visualize comminuted samples using a Leica Stereo Microscope MZ6, Germany.

X-ray diffraction (XRD) was measured with a Bruker AXS D8 Advance, Germany ($Cu_{K\alpha}$ radiation) diffractometer. Rietveld analysis was made using TOPAS software. Crystallite size of B_4C was extracted (Table 1).

Density of the samples was measured by the Archimedes method using ethanol media.

Consolidation curves were measured in-situ by SPS machine. After subtracting the curve obtained under SPS conditions of the empty graphite-mold, kinetic model was applied as explained in Section 3.2.1.

3. Results and discussion

3.1. Preliminary experiments

Samples U and V were SPSed under the same regime, but in Ar and N_2 atmosphere, respectively. Dynamic SHPB stress–strain curves are different (Fig. 1a) and, most striking is that, when heating under N_2 as for sample V, ε_{max}, σ_{max} and S are higher (Table 1). Sample V shows also higher static data, HV and K_{1c}, than for sample U SPS-ed in Ar. Improvement of static properties for SPS under N_2 was observed earlier [10]. Next, for sample Z we expanded heating time up to 1100 °C in N_2 to 20 min and from 1100 to 1800 °C heating was done in Ar. Remarkable is that HV, σ_{max} and S are not much different between U and Z samples, while ε_{max} and K_{1c} are larger for sample Z. Noteworthy, SPS in N_2 improved consolidation behavior since relative density was slightly higher for samples V (91%) and Z (93.8%) than for sample U SPS-ed in Ar (89%). Crystallite size for U, V and Z was approximately constant (~100 nm). This preliminary experiment indicates that N_2 introduction during SPS is essential to control SHPB parameters. It also suggests that interplay between reactive and sintering processes should be carefully designed and controlled during SPS processing. To do so, all our samples A–C, A*, B*, (Table 1) were prepared in nitrogen and SPS uniaxial pressure was applied gradually reaching 30, 60 or 100 MPa during heating for 25 or 40 min (Table 1).

3.2. Optimization process

For samples A–C with a SPS heating time of 25 min, enhancement of pressure (P) from 30 (sample A) to 60 MPa

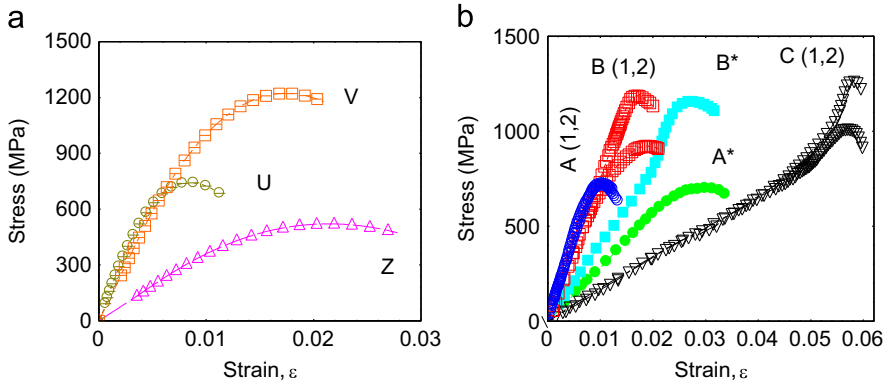

Fig. 1. SHPB stress–strain curves for different samples (Table 1).

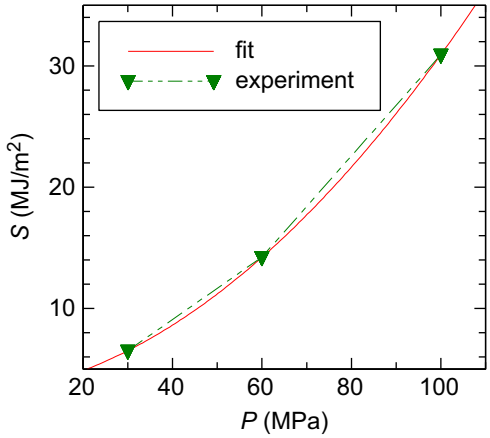

Fig. 2. Dynamic SHPB toughness vs. maximum applied pressure during SPS processing (samples A, B, C).

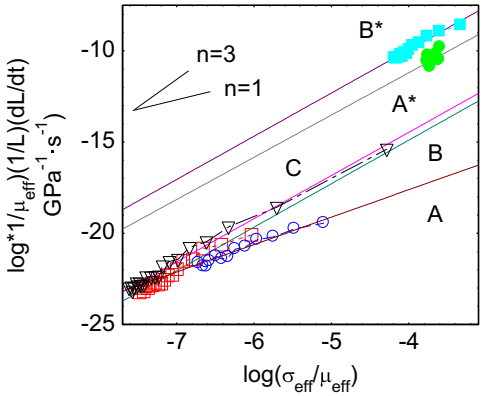

Fig. 3. Application of kinetic consolidation model (see text) to estimate n-value for A–C, A* and B* samples during SPS.

(sample B) strongly increases σ_{max}. This is accompanied by noticeable HV increase (Table 1) and an increase in relative density (from 90.5% for sample A to 95% for sample B). Static fracture toughness K_{1c} increases. Also some increase can be observed for ε_{max}. However, the increase of ε_{max} from samples A to B is rather small when compared to increase for samples C (Table 1, Fig. 1b). From 30 to 100 MPa, dynamic toughness versus SPS pressure, $S(P)$, increases following a slow upw ard parabolic dependence ($S=0.0023P^2+0.0496P+2.96$). Such dependence (Fig. 2) is due to a stronger increase of ε_{max} than of σ_{max} at higher P. Sample C shows the highest relative density (98%). From 60 to 100 MPa, HV almost does not change and K_{1c} continues to increase. Few observations of much interest are:

(i) The increase of HV somehow correlates with the increase of $\sigma_{max,}$ while for relatively constant HV the increase of K_{1c} correlates with ε_{max}.

(ii) Among the reasons for S-enhancement is the increase of relative density. This statement is partially valid and situation is more complex. For example, for samples A* and B* observation (i) regarding HV–σ_{max} relationship also applies although σ–ε curves are located at higher ε_{max} than for A and B samples. At the same time, for samples A* and B* relative densities are 94.5 and 95.2%, respectively, i.e. relative density values are not as different as for samples A (90.5%) and B (95%). They are also comparable with the values for sample B. Result that nitrogen, owing to a longer SPS heating time improves on the one hand consolidation processes and, on the other hand, also enhances ε_{max} leading to a higher S, means that nitrogen is inducing some kind of dynamic plasticity. We believe that observed plasticity is related to grain boundaries modification with formation of phases in the B–C–N–O system (see Section 3.2.2). This influences both processes of sintering and toughening, but the level of influence on each process is different and depends on SPS processing conditions. Such difference provides the possibility of microstructure refinement that allows some level of mechanical properties independent control.

3.2.1. Consolidation aspects

First we shall look on consolidation process and the approach used for hot-pressing [14,15] will be considered reasonable to describe SPS:

$$\frac{1}{\mu_{eff}}\dot{\rho} = K\frac{\exp(-E/RT)}{T}\left(\frac{\sigma_{eff}}{\mu_{eff}}\right)^n, \quad (1)$$

where $\dot{\rho}$ is $1/L$ (dL/dT), dL/dT is the shrinkage rate, L is shrinkage, μ_{eff} is the shear modulus of the powder bed, σ_{eff} is the effective stress on the powder bed, K is a constant described in Ref. [14], and n is the stress exponent. In Eq. (1), σ_{eff} and μ_{eff} are evaluated according to [14]:

$$\mu_{eff} = \frac{E_{th}}{2(1+\nu_{eff})}\frac{D-D_0}{1-D_0}\ \sigma_{eff} = \frac{1-D_0}{D^2(D-D_0)}\sigma_{mac}, \quad (2)$$

where E_{th} is Young's modulus, 460 GPa [16], of the theoretically dense B_4C, ν_{eff} is the effective Poisson's ratio chosen at 0.18 [17], D_0 is the starting density of the powder compact (taken at 50% of the theoretical density at 1200 °C which is the temperature where consolidation starts), and σ_{mac} is macroscopic compaction pressure (i.e. $P=30$, 60, 100 MPa). To find the value of n, Eq. (1) is transformed for activation energy $E=$constant

$$\mathrm{In}\left(\frac{1}{\mu_{eff}}\dot{\rho}\right) = n\ \mathrm{In}\left(\frac{\sigma_{eff}}{\mu_{eff}}\right) + K_1 \quad (3)$$

where K_1 is a constant for a fixed sintering temperature. The slope of the straight line obtained when drawing Eq. (3) corresponds to n-value (Fig. 3).

Phenomenological creep models have been developed for $n=1$–5 [18–20]. The n-values obtained for our samples are presented in Table 1. The value of $n=1$ in oxide ceramics [14,15] usually corresponds to densification caused by grain-boundary sliding and diffusion. For ceramics with covalent bonds as for B_4C [20,21], n=1 corresponds to a vacancy driven diffusion mechanism under pressure which accommodates atom movement along lattice and grain-boundaries. This mechanism usually acts under relatively low-stress conditions. This situation fits the case of our sample A (n=1.5). For sample A*, P stays low

at 30 MPa as for sample A, but n=2.32 and it is similar to all the other samples B, B*, and C obtained for higher pressure of 60 or 100 MPa (n=2.3–2.4). An increase in n may suggest a change in consolidation mechanism. For example, for YSZ ceramic [14] a value of $n=2$ is accommodated by the reactions at grain-boundaries [19,20]. But, a value of $n=2$ was also determined for hot-pressing of pristine B_4C [22,23] and above mentioned vacancy driven diffusion consolidation mechanism was associated. The n-values of our samples B, C, A* and B* exceed n=2. In general, at $n \geq 3$ a dislocation-climb controlled creep mechanism is proposed. Such high n-values and corresponding mechanism are specific for metals and for covalent ceramics are not expected (unless much higher deformation loads during SPS are applied). In summary, for our samples the change in n-value mainly occurs through vacancy driven diffusion controlled by B_4C and N_2 reaction at grain boundaries. The presence of BN–B_xO_y at grain boundaries, may also contribute to consolidation mechanism.

3.2.2. Fractography analysis

Pores in samples A, B or A*, B* are playing a major role in fracturing under dynamic SHPB regime (Fig. 4, Table 1). For example, (sample B, Fig. 4c inset) one can observe crack development along lines connecting closed pores. Cracks are straight lines indicative of mostly brittle intragranular fracture mechanism, but pores can deflect cracks. The reason for this is not clear. In Fig. 4b,d,f-inset for samples A, B and B*, EDS

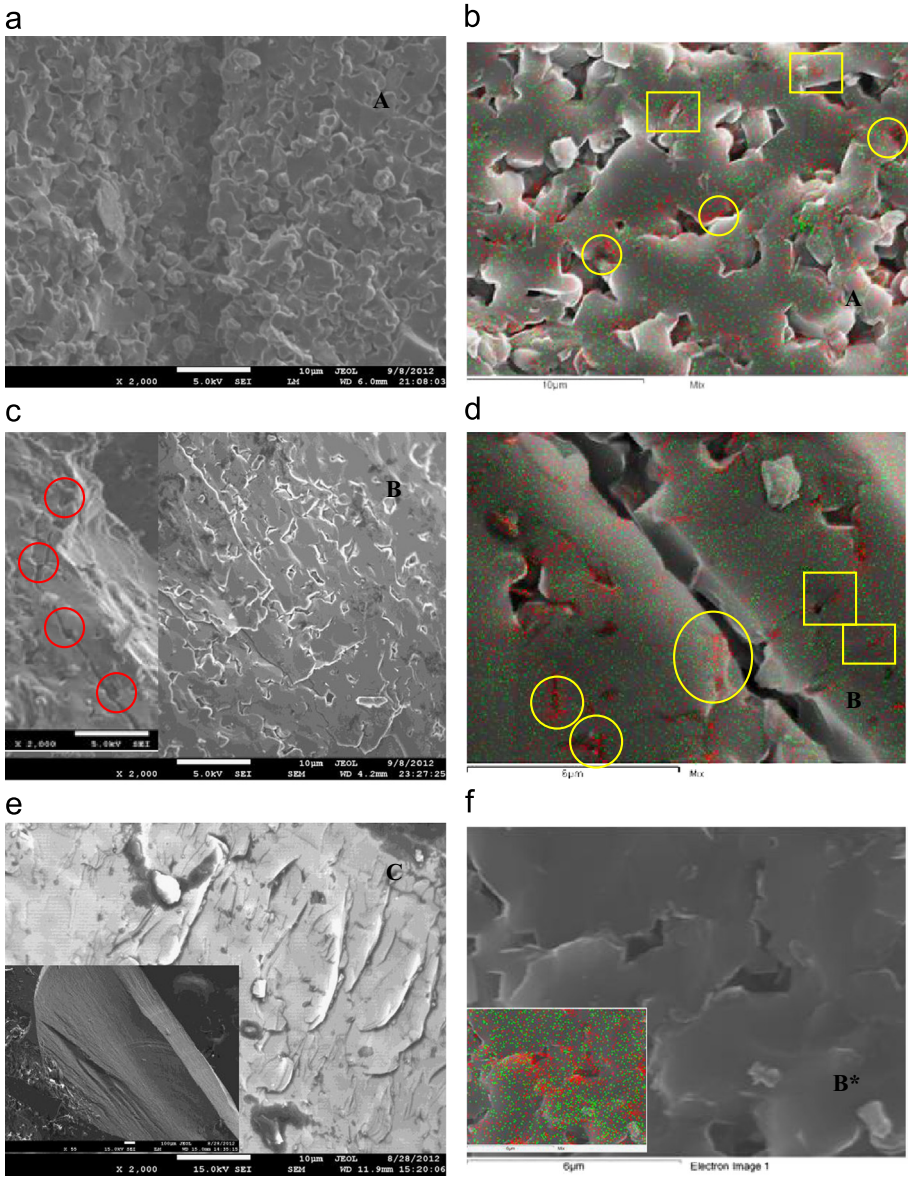

Fig. 4. SEM images (a, c, e) and SEM overlapped by EDS elemental maps (b, d, f) for nitrogen (red) and for oxygen (green) of the indicated SPSed samples (see also Table 1) after SHPB test. Inset to (c) shows crack propagation and deflection on pores marked with circles. Inset to (e) shows a general image of the surface of a needle-like piece resulting in the SHPB loading. In images (b) and (d) circles show nitrogen in close proximity to pores or on the fracture edges as they result in SHPB, while rectangles show nitrogen far away from these regions, i.e. apparently in the grains. (For interpretation of the references to color in this figure legend, the reader is referred to the web version of this article.)

elemental maps of oxygen and nitrogen suggest that segregation of these elements occurs in close proximity to pores (Fig. 4b,d, follow circles). However, segregation is also observed inside the grains (Fig. 4b,d, follow rectangles), or on their surface, or at grain boundaries (Fig. 5a) and in the absence of pores. Segregation of oxygen does not always follow segregation of nitrogen. Semi

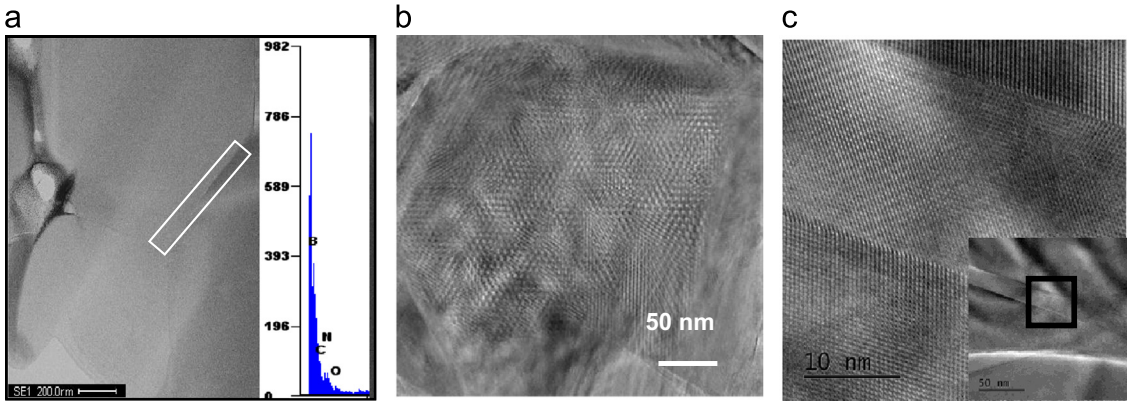

Fig. 5. TEM images sample C (after SPS): (a) B_4C grain boundary and EDS spectra showing along the boundary the presence of nitrogen and oxygen, (b) HTEM image showing crystallites within a grain and (c) HTEM image showing the presence of twins (inset is a general image at smaller magnification and square indicates the place where HTEM image was taken).

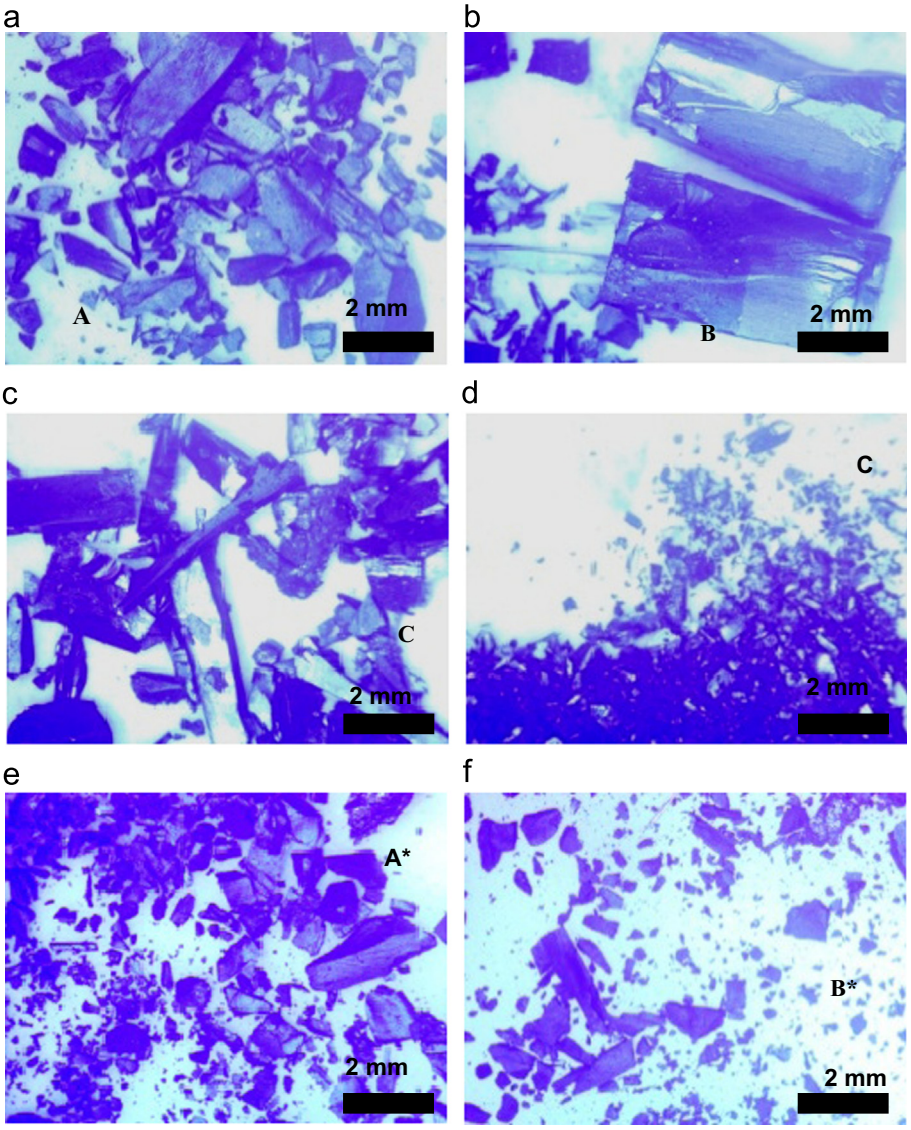

Fig. 6. Images of optical microscopy after SHPB test of (a) sample A, (b) sample B, (c) sample C, (d) sample C, (e) sample A*, and (f) sample B*.

quantitatively, EDS amount of nitrogen in the samples (averaging over about 10 measurements taken on different locations of a sample) indicates a concentration of ~1–4 wt% nitrogen for samples A–C. Considering well known experimental limitations of EDS in quantitative determination of light elements concentration, it was not possible to have a closer look into details. Nevertheless, roughly, EDS in the samples suggest that the amount of nitrogen in samples A, B and C is between 1.8 and 3.5 wt%. Variation of nitrogen can be understood as a consequence of gas trapping and squeezing during SPS when maximum applied pressure and heating regimes are changing. For cracks deflection by pores, also their shape might be critical. Pores for our material are with straight edges generating triangular or rectangular shapes especially at 30 MPa (sample A, Fig. 4a,b). Angular shapes are by definition stress concentrators. There are also pores with concave–convex round shape edges. This suggests creep flow during SPS–N_2 to fill in the closed pores toward their elimination. More such closed pores are observed for higher *P* (Fig. 4c,d,e,f) and their shapes may induce a different material's response under mechanical load.

Defects, such as well known twins in B_4C (Fig. 5b), as well as boundaries, their type, size, amount and distribution may also influence mechanical properties. Moreover, in the case of pristine B_4C, a strong tendency for disorder or solid-state transformations (e.g. with formation with amorphous bands in the B_4C grains) induced by contact pressure loads in indentation [24], scratching [25] or ballistic [26] experiments was reported. The amount of boundaries can be inferred from crystallite size and grain size. While the average grain size was in the range of 1–10 μm (Fig. 5a) for all samples being difficult to observe grains by SEM owing to high density of the samples, the average crystallite size of B_4C determined from XRD analysis and Rietveld refinement was decreasing from A to B and C and further, to a less extent, to A* and B* (Table 1). Crystallites were observed also by HTEM (Fig. 5c). A higher SPS pressure or a longer heating SPS-time is resulting in a higher amount of boundaries perhaps useful to improve toughness (see next paragraph) as in the case of Hall–Petch effect. The decrease of crystallite size can be the consequence of reaction with N_2 [10].

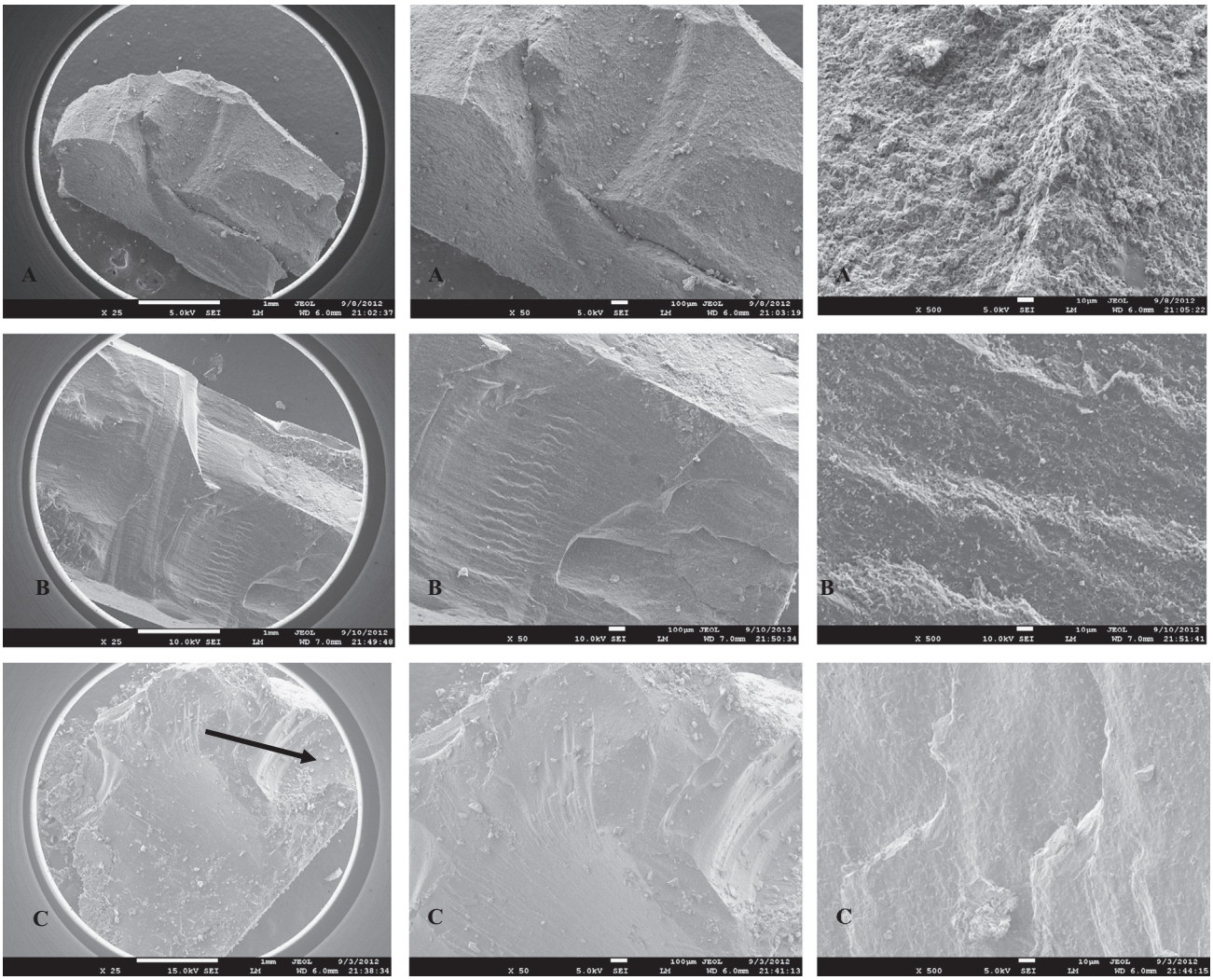

Fig. 7. SEM images at different magnifications (× 25, 50 and 500) for samples A, B and C on fractured surfaces after dynamic SHPB test. Arrow indicates a hole as a result of powder particles formation by a pull out like mechanism.

Although at present it is impossible to identify the factors and their interplay leading to a clear image of their influence on mechanical properties, observations (Table 1) from optical microscopy on samples after SHPB (Fig. 6a–f) test show an interesting tendency: broken samples with higher ε_{max} (e.g. V, Z vs. U, or C vs. A, B, or A* and B* vs. A and B, respectively) are always composed of a fine and uniform powder fraction. In ballistic tests conducted on pristine B_4C ceramic [26] obtained by hot pressing, a powder fraction was observed above a value of 850 m/s of the impact velocity. By high-resolution electron microscopy it was revealed on samples subject to impact velocities above this critical value the formation of nanoscale intragranular amorphous bands that occur parallel to specific crystallographic planes and contiguously with apparent cleaved fracture surfaces. Despite the fact that there are similarities between our results and those reported in Ref. [26], there are also notable differences. We mention here that in our case the material is a B_4C-based composite, the impact velocity in our SHPB experiments from this work is much lower than in ballistic tests and the impact velocity is constant at about 12 m/s. Therefore, the occurrence of the powder fraction after SHPB test for samples with high ε_{max} cannot be solely related to disorder and amorphous bands formation in the B_4C grains. Under presented circumstances, the occurrence of the powder fraction suggests a sort of mechanism to limit the length of the developing crack. Result resembles breakage in composites under static regime in which an inclusion phase provides some degree of plasticity through different mechanisms (deflection, arrest, boundary sliding, phase pull out, and others) influencing cracks development (e.g. as in eutectic B_4C–TiB_2 ceramic subject to bending strength measurements [27]). To have such an effect, the presence of pores is less important than the components of the composite and their relationship. Observations from this paragraph are strongly supported by fracture details of the macro surfaces visualized by SEM and presented in Figs. 7 and 8. From sample A to B and C the number of straight fracturing lines is decreasing in favor of wavy, curved and sometimes loop-like lines (Fig. 7). Compositional EDS maps for oxygen and nitrogen indicate that these elements are sometimes following the fracture lines, but not always. Hence, lines formation is not directly dependent on oxygen and nitrogen presence and it is likely that the fracture mechanism proposed for ballistic conditions [26] is also active. Wavy lines are observed as packages of apparently parallel individual lines (e.g. samples B and C in Fig. 7). The last two observations suggest the development of the lines in connection with impact propagation wave (longitudinal along the thickness of the sample and also radial). The presence of highly curved and of loop-like lines are suggesting a cracks propagation mechanism leading to a sort of pull out mechanism with formation of the fine powder fraction during SHPB tests (Fig. 6C left). The expected consequences are toughening of ceramic under SHPB dynamic load conditions (see *S* for samples A, B, C in Table 1). This mechanism is different from the brittle intragranular crack development mechanism connecting pores, presented at the beginning of this section (Fig. 4c inset): in this case lines are wavy and are not straight as for the pores-connecting situation and, furthermore, wavy lines occur without connecting pores (Fig. 7a). There are also some differences versus the mechanism encountered during static type loading such as room temperature 3-point bending test performed with an Instron 4505 apparatus, UK. For example, in Fig. 8 are shown at the same magnification fractured surfaces of sample C after SHPB and of sample B* after bending. For sample B* after bending, most of the visible fracture lines are straight and form angular patterns suggesting breakage through cleavage along certain crystallographic planes (e.g. involving twin boundaries). More general, as one can observe, the topography of the two surfaces is quite different. Details of bending tests of N_2–SPS-ed B_4C samples at room and high temperatures will be reported elsewhere.

Presented complex relationships require further systematic investigations and confirmation. Nevertheless, it is remarkable that SPS treatment in nitrogen controls 'plasticity' and, thus, also *S* (see A* vs. A and B* vs. B, Table 1). Result also suggests that a N_2–SPS treatment (40 min) as for A* and B*, but under a higher pressure, e.g. 100 MPa may push ε_{max} and *S* to higher values than in this work. Experiments are in progress.

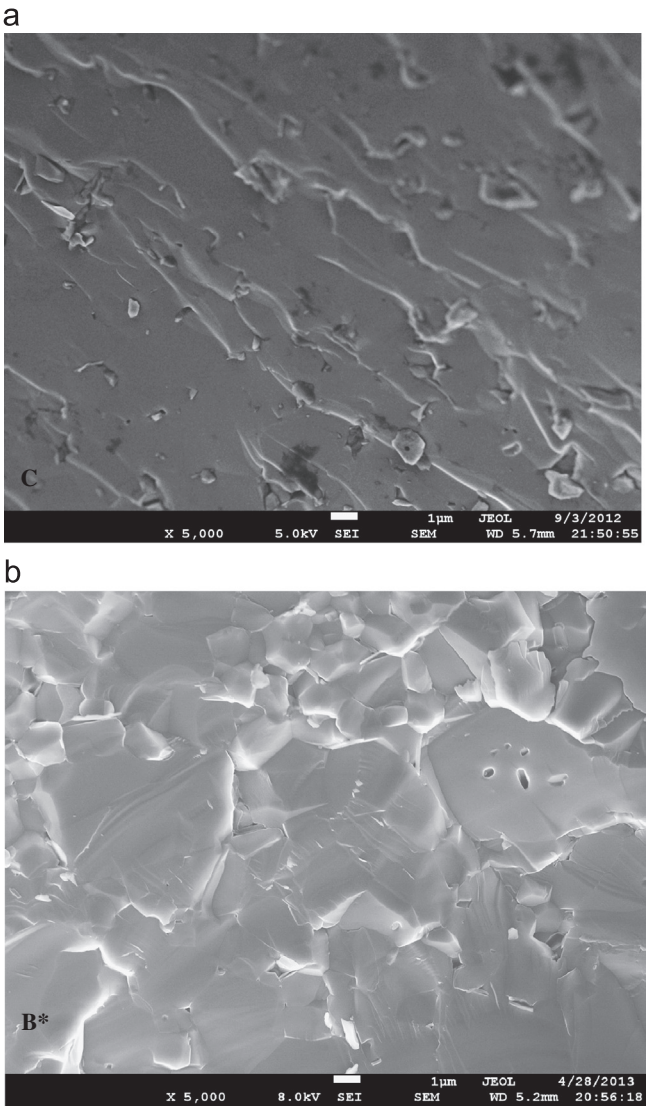

Fig. 8. SEM images taken on fractures surfaces of sample A after SHPB dynamic test (a), and of sample B* after static room-temperature bending test (b).

4. Conclusion

Our work indicates that dynamic mechanical properties of B_4C can be controlled by designing B_4C composites in which boundaries between B_4C–B_4C grains are modified. In this work, boundaries frame-structure is influenced through reactive Spark Plasma Sintering processing performed in nitrogen atmosphere. Results show that dynamic toughness can be controlled through wisely selecting thermal and pressure SPS regimes. This provides the means for further developments toward higher toughness and optimization of other mechanical properties parameters (such as ε_{max}, σ_{max}) of B_4C-based ceramic composites.

It is also inferred that certain dependencies between static and dynamic mechanical properties are possible given that their correlation with materials' structural and microstructure details will be revealed. Significant future research is required in this direction. Fracture analysis after dynamic test points on mechanisms leading to toughness improvement. Some of them resembles those specific for static loads such as cracks deflection and pull out. But, also notable differences were revealed.

Acknowledgment

Authors acknowledge support through TL/9010103762 and TL/9010101538-04 projects, Singapore.

References

[1] A.K. Suri, C. Subramanian, J.K. Sonber, T.S.R.Ch. Murthy, Synthesis and consolidation of boron carbide: a review, International Materials Reviews 55 (2010) 4.
[2] F. Thevenot, Boron carbide – a comprehensive review, Journal of the European Ceramic Society 6 (1990) 205.
[3] S.M. Walley, Historical review on high strain rate and shock properties of ceramics relevant to their application in armour, Advances in Applied Ceramics 109 (2010) 446.
[4] J.E. Field, S.M. Walley, W.G. Proud, H.T. Goldrein, C.R. Siviour, Review of experimental techniques for high rate deformation and shock studies, International Journal of Impact Engineering 30 (2004) 725.
[5] F. Ye, Z. Hou, H. Zhang, L. Liu, Densification and mechanical properties of spark plasma sintered B4C with Si as a sintering aid, Journal of the American Ceramic Society 93 (2010) 2956.
[6] L.S. Walker, V.R. Marotto, M.A. Rafiee, N. Koratkar, E. Corral, Toughening in graphene ceramic composites, ACS Nano 5 (2011) 3182.
[7] S.H. Risbud, J.R. Groza, M.J. Kim, Clean grain boundaries in aluminum nitride ceramics densified without additives by a plasma-activated sintering process, Philosophical Magazine B—Physics of Condensed Matter, Statistical Mechanics, Electronic, Optical and Magnetic Properties 69 (1994) 525.
[8] A. Pettersson, P. Magnusson, P. Lundberg, M. Nygren, Titanium–titanium diboride composites as part of a gradient armour material, International Journal of Impact Engineering 32 (2005) 387.
[9] G. Bernard-Granger, A. Addad, G. Fantozzi, G. Bonnefont, Ch. Guizard, D. Vernat, Spark plasma sintering of a commercially available granulated zirconia powder: Comparision with hot-pressing, Acta Materialia 58 (2010) 3390.
[10] O. Vasylkiv, H. Borodianska, P. Badica, S. Grasso, Y. Sakka, A. Tok, L. T. Su, M. Bosman, J. Ma, High hardness B_aC_b–(B_xO_y/BN) composites with 3D mesh-like fine grain-boundary structure by reactive spark plasma sintering, Journal of Nanoscience and Nanotechnology 12 (2012) 959.
[11] U.S. Lindholm, Some experiments with the split Hopkinson pressure bar, Journal of the Mechanics and Physics of Solids 12 (1964) 18.
[12] S. Sarva, S. Nemat-Nasser, Dynamic compressive strength of silicon carbide under uniaxial compression, Materials Science and Engineering A 317 (2001) 140.
[13] K. Niihara, R. Morena, D.P.H. Hasselman, Evalution of K_{1C} of brittle solids by the indentation method with low crack-to-indent ratios, Journal of Materials Science Letters 1 (1982)13 1 (1982).
[14] G. Bernard-Granger, C. Guizard, Spark plasma sintering of a commercially available granulated zirconia powder: I. Sintering path and hypotheses about the mechanism(s) controlling densification, Acta Materialia 55 (2007) 3493.
[15] H. Borodianska, D. Demirskyi, Y. Sakka, P. Badica, O. Vasylkiv, Grain boundary diffusion driven spark plasma sintering of nanocrystalline zirconia, Ceramics International 38 (2012) 4385.
[16] G.R. Johnson, T.J. Holmquist, Response of boron carbide subjected to large strains, high strain rates, and high pressures, Journal of Applied Physics 85 (1999) 8060.
[17] S.P. Dodd, G.A. Saunders, B. James, Temperature and pressure dependences of the elastic properties of ceramic boron carbide (B4C), Journal of Materials Science 37 (2002) 2731.
[18] M.F. Ashby, R.A. Verrall, Diffusion-accommodated flow and superplasticity, Acta Materialia 21 (1973) 149.
[19] B. Burton, G. Knowles, The relationship between dislocation recovery creep and vacancy diffusion creep, Philosophical Magazine A—Physics of Condensed Matter, Structure, Defects and Mechanical Properties 44 (1981) 987.
[20] W.R. Cannon, T.G. Langdon, Creep of ceramics.1. mechanical characteristics, Journal of Materials Science 18 (1983) 1.
[21] T.G. Abzianidze, A.M. Eristavi, S.O. Shalamberidze, Strength and creep in boron carbide (B4C) and aluminum dodecaboride (alpha AlB(12)), Journal of Solid State Chemistry 154 (2000) 191.
[22] M.S. Koval'chenko, Yu.G. Tkachenko, V.V. Koval'chuk, D.Z. Yurchenko, S.V. Satanin, A.I. Kharlamov, Structure and properties of hot-pressed boron carbide base ceramics, Soviet Powder Metallurgy and Metal Ceramics 29 (1990) 523.
[23] I.T. Ostapenko, V.V. Slezov, R.V. Tarasov, N.F. Kartsev, V.P. Podtykan, Densification of boron carbide powder during hot pressing, Soviet Powder Metallurgy and Metal Ceramics 18 (1979) 312.
[24] V. Domnich, Y. Gogotsi, M. Trenary, T. Tanaka, Nanoindentation and Raman spectroscopy studies of boron carbide single crystals, Applied Physics Letters 81 (2002) 3783.
[25] D. Ge, V. Domnich, T. Juliano, E.A. Stach, Y. Gogotsi, Structural damage in boron carbide under contact loading, Acta Materialia 52 (2004) 3921.
[26] M. Chen, J.W. McCauley, K.J. Hemker, Shock-induced localized amorphization in boron carbide, Science 299 (2003) 1563.
[27] I. Bogomol, P. Badica, Y. Shen, T. Nishimura, P. Loboda, O. Vasylkiv, Room and high temperature toughening in directionally solidified B_4C–TiB_2 eutectic composites by Si doping, Journal of Alloys and Compounds 570 (2013) 94.